



Fermiology and electron-phonon coupling in the 2H and 3R polytypes of NbS₂Zakariae El Youbi ^{1,2}, Sung Won Jung,¹ Christine Richter,^{2,3} Karol Hricovini,^{2,3} Cephise Cacho,¹ and Matthew D. Watson ^{1,*}¹*Diamond Light Source, Harwell Campus, Didcot, OX11 0DE, United Kingdom*²*Laboratoire de Physique des Matériaux et des Surfaces, CY Cergy Paris Université, 5 mail Gay-Lussac, 95031 Cergy-Pontoise, France*³*Université Paris-Saclay, CEA, CNRS, LIDYL, 91191, Gif-sur-Yvette, France*

(Received 16 December 2020; accepted 18 March 2021; published 2 April 2021)

We investigate the electronic structure of the 2H and 3R polytypes of NbS₂. The Fermi surfaces measured by angle-resolved photoemission spectroscopy show a remarkable difference in size, reflecting a significantly increased band filling in 3R-Nb_{1+x}S₂ compared to 2H-NbS₂, which we attribute to the presence of additional interstitial Nb, which act as electron donors. Thus, we find that the stoichiometry, rather than the stacking arrangement, is the most important factor in the difference in electronic and physical properties of the two phases. Our high resolution data on the 2H phase shows kinks in the spectral function that are fingerprints of the electron-phonon coupling. However, the strength of the coupling is found to be much larger for the sections of bands with Nb $4d_{x^2-y^2,xy}$ character than for the Nb $4d_{3z^2-r^2}$. Our results provide an experimental framework for interpreting the two-gap superconductivity and latent charge density wave in 2H-NbS₂.

DOI: [10.1103/PhysRevB.103.155105](https://doi.org/10.1103/PhysRevB.103.155105)**I. INTRODUCTION**

Transition metal dichalcogenides (TMDs) are well-known for hosting a variety of instabilities arising from the interplay of electron-electron and electron-phonon coupling. Particularly rich phenomena are found in the metallic (V, Nb, Ta)(S, Se, Te)₂ family, including Mott-insulating phases, superconductivity, and numerous charge density waves (CDWs) [1–4]. As a well-known example, 2H-NbSe₂ exhibits a $\sim 3 \times 3$ CDW and also superconducts at 7.2 K [5–8]. Several of these layered van der Waals materials favor the trigonal prismatic coordination of the transition metal, but there is an additional degree of freedom in the interlayer stacking pattern (e.g., 2H, 4H, 3R polytypes [9]), leading to further variety of the novel electronic ground states.

Unlike most other members of the (V, Nb, Ta)(S, Se, Te)₂ family, 2H-NbS₂ does not undergo any structural instability [10]. Nevertheless, a phonon mode exhibits significant softening with temperature [11], and 2H-NbS₂ can be viewed as being close to a lattice instability. This presents an interesting theoretical challenge, as naïve density functional theory (DFT) calculations would predict a lattice instability [12], and the absence of any CDW phase is attributed to the anharmonic phononic effects [11,13]. 2H-NbS₂ is also a prototypical two-gap superconductor below $T_c = 6.2$ K, as evidenced by tunneling spectroscopy [14], Andreev reflections [15], and heat capacity measurements [16]. Despite this, the experimental electronic structure of bulk 2H-NbS₂ has hardly been

explored [17]. Meanwhile, an alternative stacking structure, the noncentrosymmetric 3R phase, has been reported for some time [18,19] but little is known about its electronic structure or how and why its properties differ from the 2H phase.

Here, we examine the low-energy electronic structure of 2H-NbS₂ and 3R-Nb_{1+x}S₂ combining angle-resolved photoemission spectroscopy (ARPES) and DFT calculations. The measured Fermi surfaces reveal a striking difference in size, implying a significantly greater band filling in the 3R phase. We attribute this difference to additional Nb interstitials in the 3R phase, which act as electron donors. This difference is likely to move the 3R phase away from any latent instabilities and may explain the absence of superconductivity in this phase. Finally, the high-resolution data on the 2H phase reveals that the electron-phonon coupling is highly dependent on the orbital character of the bands, which naturally links to the two-gap superconductivity.

II. METHODS

Single crystals were obtained commercially (HQ Graphene, Groningen) and cleaved *in situ*. ARPES measurements were performed at the I05 beamline of Diamond Light Source [20], using photon energies in the range 30–240 eV, at sample temperatures below 10 K. DFT calculations were performed within the WIEN2K package [21], using the modified Becke-Johnson functional [22] and accounting for spin-orbit coupling, as further detailed in the Supplemental Material (SM) [23].

III. RESULTS**A. Comparison of the 2H and 3R phases**

In the 2H phase (space group 194, $P6_3/mmc$), each NbS₂ layer is rotated by 180° with respect to the layer below it

*matthew.watson@diamond.ac.uk

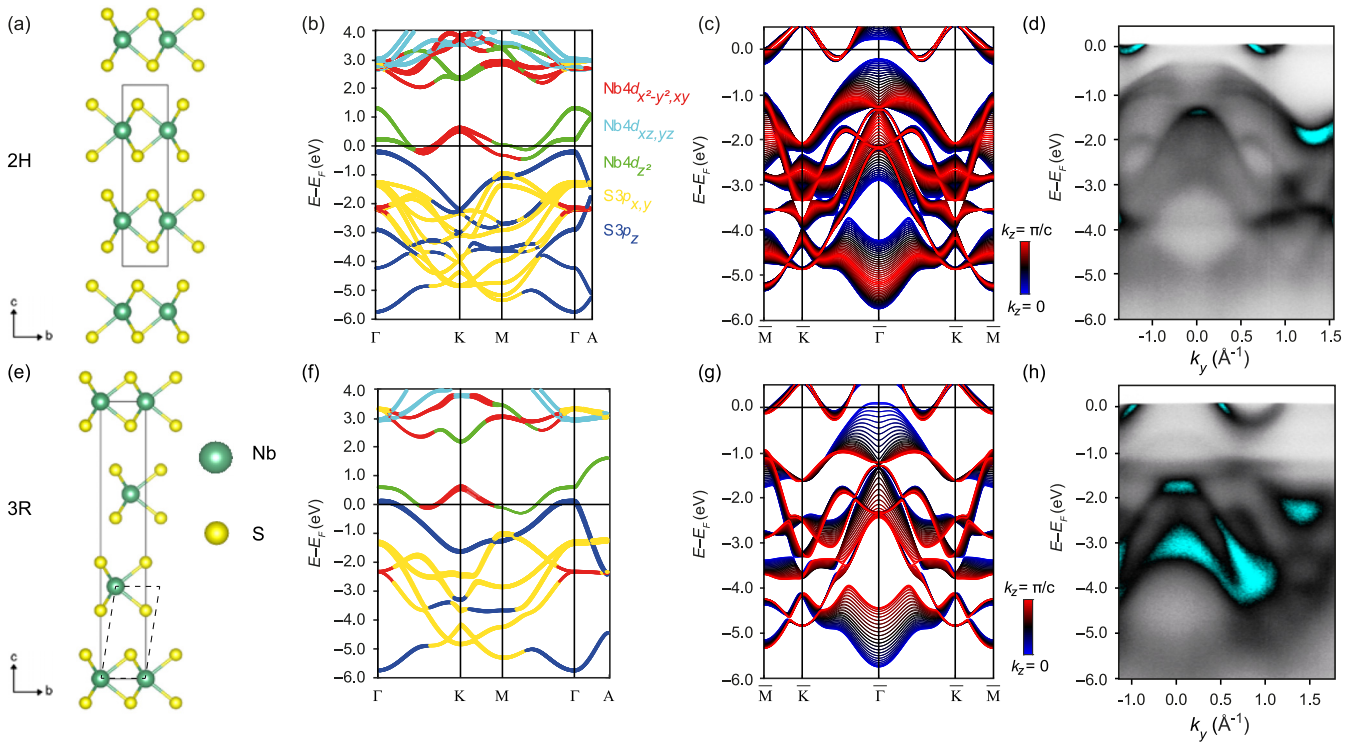


FIG. 1. Crystalline and electronic structure of $2H$ - NbS_2 and $3R$ - NbS_2 . (a), (e) Crystal structures, showing the different stacking modes. (b), (f) DFT calculations with orbital character projection of the valence and conduction bands for $2H$ - NbS_2 (b) and $3R$ - NbS_2 (f). (c), (g) k_z projection of the DFT band structure along the experimentally relevant M - K - Γ - K - M (L - H - A - H - L) direction for $2H$ - NbS_2 (c) and $3R$ - NbS_2 (g). (d), (h) Overview ARPES spectra showing valence band dispersions. Data measured along Γ - K direction at $h\nu = 79$ eV and $h\nu = 68$ eV for $2H$ - NbS_2 (d) and $3R$ - NbS_2 (h), respectively, using LH (p) polarized light.

[Fig. 1(a)]. Due to the trigonal prismatic coordination of the Nb, a single layer would not possess inversion symmetry, however, in the $2H$ phase a center of inversion symmetry exists between the layers [24–26]. Contrastingly, in the $3R$ phase (space group 160, $R3m$) shown in Fig. 1(e), there is no rotation but rather each layer is translated by a third of a lattice constant in the b direction, with respect to the layer below. This stacking structure does not contain any points of inversion.

In our DFT calculations in Figs. 1(b) and 1(f), we find twice as many bands in the $2H$ phase compared to the $3R$ phase, since the $2H$ unit cell contains two formula units, while the $3R$ phase contains one (in the primitive unit cell). The height of the Brillouin zone (i.e., Γ - A) in the $2H$ phase is half that of the $3R$ phase. Around the K point, in the $2H$ phase the bands near E_F with Nb $4d_{x^2-y^2,xy}$ character (red) are split due to combination of interlayer hopping and the spin-orbit coupling, as discussed in numerous studies of $2H$ - MoS_2 [27–29], $2H$ - WSe_2 [26,30], and $2H$ - NbSe_2 [31]. However, the Nb $4d_{3z^2-r^2}$ orbital (green) is more significantly affected by interlayer hopping terms, leading to a large band splitting of ~ 1 eV at the Γ point above E_F in Fig. 1(b). For the in-plane S $3p_{x,y}$ valence bands (yellow), we find a small splitting of the band dispersions in the $2H$ phase compared to the $3R$, since for these orbitals the interlayer hopping terms are relatively weak compared to the in-plane hoppings. In contrast, the S p_z orbitals (blue) disperse strongly in the out-of-plane directions, and are most strongly sensitive to the stacking sequence.

In both phases, therefore, there are both quasi-2D and rather 3D valence bands, as highlighted in the k_z projection of the band structure [Figs. 1(c) and 1(g)]. This is a helpful representation of the DFT band structure for comparison with ARPES measurements due to the nonconservation of k_z in the photoemission process, which leads to an effective integration over a range of k_z values [26,32–34]. In the overview ARPES spectra of the $2H$ phase in Fig. 1(d), the valence bands closely resemble the k_z -projected calculations, including sharp features from quasi-2D states, and broad features from 3D bands. In the case of the $3R$ phase, however, the agreement is notably worse. First, the data quality in Fig. 1(h) is lower; none of the features are as sharp as in the $2H$ phase, with a significantly higher background signal. Second, there is evidence for a flat state at $E_B = -1.2$ eV, not present in the calculations, which is indicative of some form of localized impuritylike state. Third, the Nb $4d$ -derived bands at the Fermi level have a substantially larger filling than in the calculations.

To further understand the difference between the two phases, in Fig. 2 we consider the Fermi surfaces. The DFT calculations of the Fermi surfaces in the two cases are broadly similar, as in both cases quasi-2D barrels appear, centered around the Γ and K points [Figs. 2(a) and 2(e)]. The interlayer hopping in the $2H$ phase plays an important role in creating a splitting of inner and outer barrels around K . However there is no such splitting term in the $3R$ phase and the splitting is a spin splitting, allowed due to the absence of inversion symmetry [23]. In Figs. 2(b) and 2(f), we present simulations of the in-plane Fermi surfaces after averaging over the entire

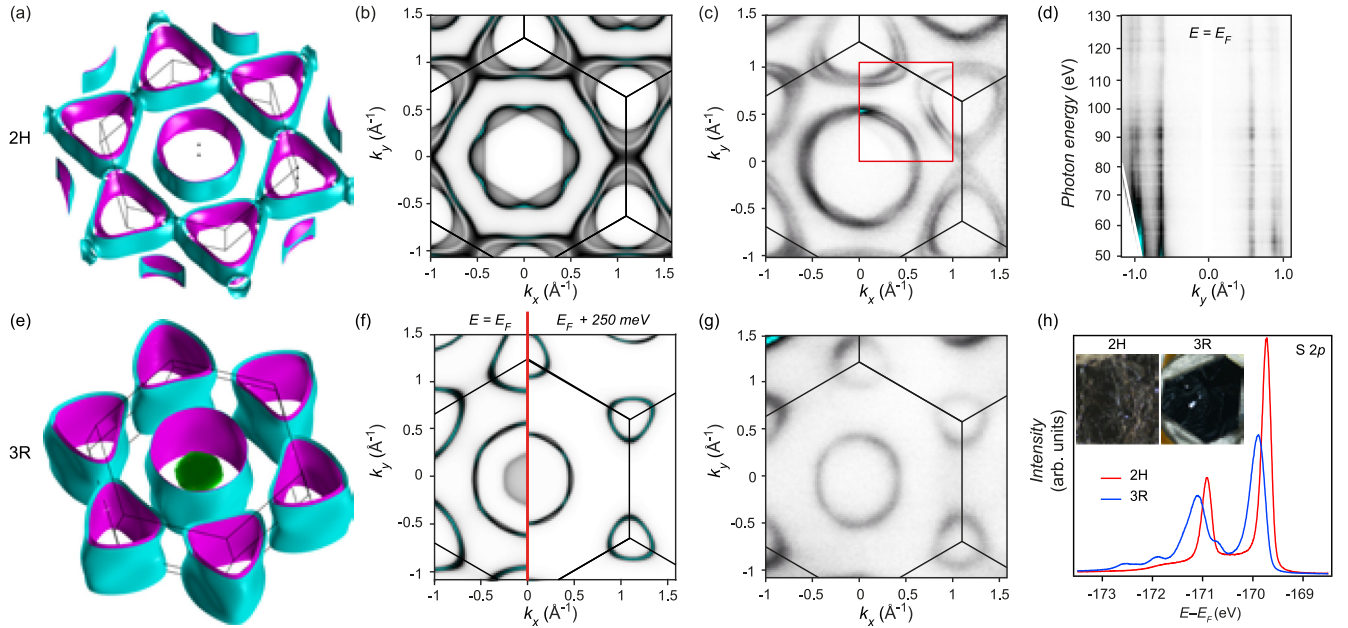


FIG. 2. Fermiology of $2H$ - NbS_2 and $3R$ - NbS_2 . (a), (e) Calculated 3D Fermi surface of (a) $2H$ - NbS_2 and (e) $3R$ - NbS_2 . (b), (f) Simulated Fermi surfaces obtained by averaging over the whole Brillouin zone width in the k_z direction for $2H$ - NbS_2 (b) and $3R$ - NbS_2 (f). In the latter, a section is simulated at 250 meV above the natural Fermi level. (c), (g) Fermi surface measured at a photon energy $h\nu = 79$ eV (inset, 42 eV) for $2H$ - NbS_2 (c), and $h\nu = 120$ eV for $3R$ - NbS_2 (g). (d) Photon energy-dependent ARPES of $2H$ - NbS_2 from 50 to 130 eV, plotting MDCs at E_F along K - Γ - K (H - A - H) direction as a function of photon energy, showing the quasi-2D nature of electronic states with a consistently resolved splitting of the K barrel bands. (h) S $2p$ core levels of $2H$ - NbS_2 (red) and $3R$ - NbS_2 (blue) using a photon energy $h\nu = 240$ eV, showing clearly additional satellites in the $3R$ phase. Inset shows microscope images of the single crystals used in this work.

k_z axis [35]. The measured Fermi surface in the $2H$ phase, Fig. 2(c), is broadly comparable with the calculations. Notably, the band splitting around the K barrels is reproduced, and we can also resolve the two separate bands forming the Γ barrel, with the inner displaying a strong hexagonal warping. The most noticeable difference is that, experimentally, the triangular barrels around K form closed pockets (similar to $2H$ - NbSe_2 [7,31]), while in our calculation the outer K barrels connect near the M points. We attribute this to a limit to the accuracy of the functional, rather than any off-stoichiometry of the $2H$ sample. The more advanced GW calculations of Ref. [36] similarly found smaller, closed, K barrels, along with slightly expanded Γ barrels (see SM for detailed comparison [23]). Experimentally, we find that the observed Fermi surface appears highly two-dimensional, with very little variation observed in the photon energy dependence in Fig. 2(d).

However, in the measured Fermi map of $3R$ - NbS_2 [Fig. 2(g)], the Γ and K barrels of the Fermi surface are found to be both significantly smaller compared to the calculations [Fig. 2(f), $k_x < 0$]. This is consistent with the increased filling of the band in Fig. 1(h), and is indicative of a large shift in the chemical potential. Instead, the data closely resembles the simulation in Fig. 2(f), $k_x > 0$, where the Fermi level is set 250 meV above the natural Fermi level of the calculation. This implies a significant amount of extra charge in the system; in the calculation, a rigid shift of 250 meV as shown corresponds to 0.483 extra electrons per unit cell.

The experimental data therefore point toward an important role for the stoichiometry in determining the electronic structure differences between the two polytypes. While the $2H$

phase is reported to exist only as stoichiometric NbS_2 , the $3R$ phase is known to host additional Nb interstitials, resulting in a stoichiometry of the form $3R\text{-Nb}_{(1+x)}\text{S}_2$. According to Ref. [18], the range of stability of the $3R$ phase is $0.07 < x < 0.18$; consistent with this, energy-dispersive x-ray spectroscopy measurements on our $3R$ samples indicate $x \approx 0.13$ [37]. According to Ref. [19], interstitial atoms are more favorably incorporated in the $3R$ phase due to the relatively longer distance between these extra Nb atoms and the in-plane Nb sites. Thus, the fact that there exists two polytypes at all is intimately related to the stoichiometry. These Nb interstitials act as electron donors, giving an increased overall filling of the d shell of the Nb in the main layers. Taking the ratio of the apparent extra electrons in the Fermi surface to x , we can estimate that each interstitial Nb donates ~ 3.7 electrons on average. The interstitial sites also act as local impurity potentials, explaining the broadening and extra background in the ARPES data in, e.g., Fig. 1(h).

The presence of interstitial Nb can also be inferred from the S $2p$ core level spectra in Fig. 2(h). In the case of the $2H$ phase, a sharp doublet is observed, consistent with spin-orbit split $2p_{1/2}$ and $2p_{3/2}$ states from a single chemical site. However, in the $3R$ phase, there are additional minority peaks, arising from S atoms in a chemical environment with more than the normal three nearest-neighbor Nb atoms, due to the interstitial Nb occupancy. The main doublet is also broadened, reflecting electronic inhomogeneity caused by the partial filling of the interstitial sites. Moreover, the main doublet is shifted by ~ 180 meV, a chemical shift related to the overall chemical potential and average orbital fillings. It is worth remarking that

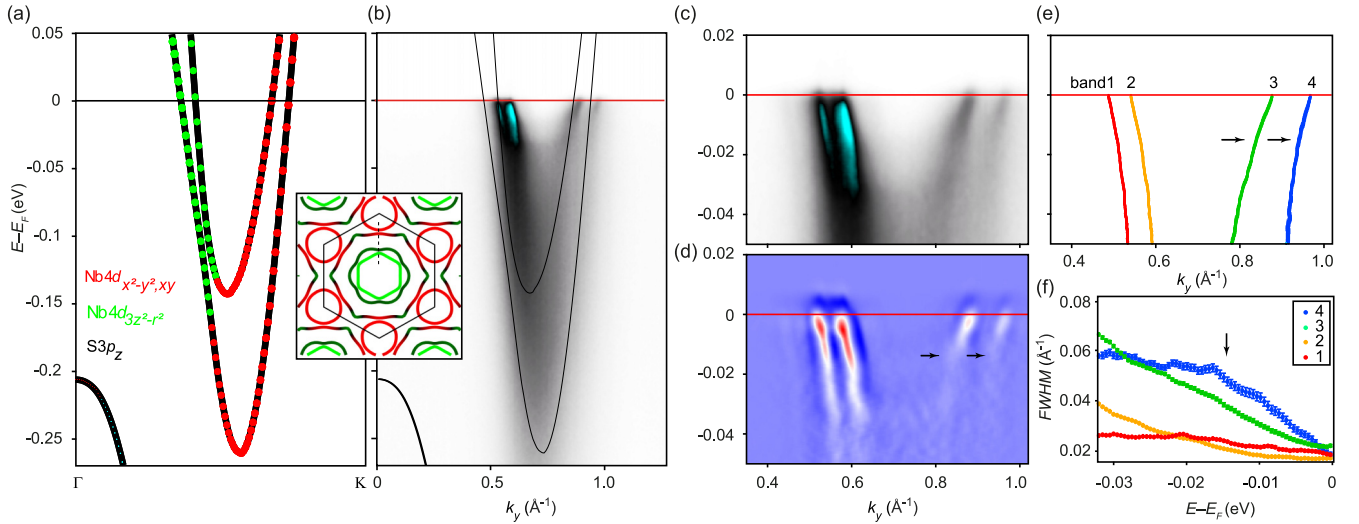


FIG. 3. Electron-phonon coupling in $2H\text{-NbS}_2$. (a) Calculated band dispersion along ΓK direction, with orbital character projection. Inset: Calculated 2D Fermi surface; the thick black line indicates the experimental cut analyzed in (c)–(f). (b) ARPES data of the valence band dispersion along ΓK , measured at a photon energy $h\nu = 30$ eV, overlaid with DFT calculations for comparison. (c) Closer look at the data near E_F and (d) the curvature plot of the data, highlighting kinks in the spectral function. (e) Momentum distribution curve (MDC) fitting of the data using a multi-Lorentzian peak function and (f) peak widths of the four bands.

the two polytypes also have different physical appearances; although both black and metallic looking, the off-stoichiometric $3R$ phase forms as beautiful platelike single crystals with clear crystal facets, while the $2H$ phase forms thin, flaky samples usually without clear facets. Thus, NbS_2 exemplifies the mantra of not judging by appearances.

B. Electron-phonon coupling in the $2H$ phase

Although neither phase undergoes any structural phase transition, $2H\text{-NbS}_2$ is considered to be on the brink of a CDW-like transition [11–14,16,38–40], while a CDW does stabilize in the closely related $2H\text{-NbSe}_2$ at 33.5 K. It is generally acknowledged that the CDWs in this family of materials cannot be explained by electronic nesting alone and it is important to consider the momentum dependence of the electron-phonon interaction, which itself is related to the orbital character of the bands [5,7,8,41–44]. For the calculated bands along ΓK in Fig. 3(a), there is a crossover in orbital character between the doublets corresponding to the Γ barrels (mainly $\text{Nb } 4d_{3z^2-r^2}$) and the K barrels (mainly $\text{Nb } 4d_{x^2-y^2,xy}$, see also Fig. S2 [23]). The experimental spectral function in Fig. 3(b) shows a significantly different impact of electron-phonon coupling at the two pairs of Fermi crossings, with the second pair of crossings (corresponding to the K barrels) exhibiting a clear kink structure, characteristic of a strong electron-phonon interaction, whereas for the first pair (Γ barrels) the effect is much less prominent.

For a more quantitative analysis, we performed a fitting analysis to extract the band positions in Fig. 3(e). From this, we identify a kink energy of -15 meV for the K barrels; the deviation of the bands around this energy can also be visualized in the curvature plot in Fig. 3(d). Meanwhile, the inner bands have a change of slope around -20 meV, but this is a more subtle effect. A quantitative measure of electron-phonon coupling is the renormalization of the Fermi velocity,

$\lambda = v_F(\text{bare})/v_F(\text{exp}) - 1$ [45]. If we assume the $v_F(\text{bare})$ values from DFT (see SM for discussion [23]), we find a clear dichotomy between the innermost band 1, with $\lambda \approx 0.51$, and the outer crossings of the K barrel with $\lambda \approx 2.32$ for band 3 and $\lambda \approx 2.59$ for band 4. Additionally, in Fig. 3(f) we show a dichotomy in the energy-dependent linewidths, as the broadening of the K barrels increase much faster with binding energy than the Γ barrels. The outermost band 4 shows the fastest rise, consistent with having the strongest coupling, and also shows a saturation of the linewidth coinciding with the kink energy [45].

Taken together, this evidence strongly suggests that in $2H\text{-NbS}_2$, the electron-phonon coupling depends crucially on the orbital character of the bands, and for the ΓK dispersion analyzed here, the λ value is up to $\sim 4\text{--}5$ times larger for the section with $\text{Nb } 4d_{x^2-y^2,xy}$ character than for the $\text{Nb } 4d_{3z^2-r^2}$. Our experiments are highly consistent with the calculations of Ref. [13], who took the electron-phonon interaction into consideration and also found a significantly larger interaction strength on the sections of the K barrel closest to the K points, correlating closely with the $\text{Nb } 4d_{x^2-y^2,xy}$ orbital character. This has important implications for the superconductivity and our data gives strong experimental support for the scenario of Ref. [13], where the inner Γ sheets with weaker el-ph coupling are cold areas corresponding to the smaller gap, while the straight sections of the K barrels are hot regions developing a larger gap, explaining the overall gap structure with two characteristic energy scales [14,15].

IV. DISCUSSION

Recapping the results on $3R\text{-Nb}_{(1+x)}\text{S}_2$, we showed that the prevalence of donor-type interstitials leads to a significant chemical potential shift by approximately 250 meV, compared to either the calculations for stoichiometric $3R\text{-NbS}_2$ or compared to the $2H$ phase. This implies an extra population of the

Nb $4d$ bands that dominate the Fermi surface, an increased filling of ~ 0.48 extra electrons per Nb. The resulting Fermi surface pockets are still holelike but substantially smaller in area, and calculations indicate a reduced electronic density of states (DOS) at E_F by a factor of ~ 2 at this doping level (SM). A reduced DOS in the $3R$ phase is, furthermore, consistent with a magnetic susceptibility that is lower by a factor of 2–3 in the $3R$ phase compared with the $2H$ phase, in the Pauli paramagnetic regime [18]. While a full treatment would also take into account differences in phononic structure between the two stacking sequences, the reduced electronic DOS alone is already likely to move the doped $3R$ system further away from the latent structural instabilities found in the $2H$ phase [11]. Similarly, in terms of superconductivity, the lower electronic DOS in the $3R$ phase will be a factor in lowering T_c to the point that no superconductivity has yet been reported in the $3R$ phase. The calculations using Eliashberg theory in Ref. [46] found a reduction of T_c by at least a factor of 3 for a positive chemical potential shift of 150 meV in $2H$ -NbS₂, while our $3R$ phase sample is effectively shifted by 250 meV. The interstitial Nb sites will also act as impurity scattering sites, explaining the broader features observed by ARPES here. This is consistent with the high density of atomic-scale imperfections observed in STM measurements on $3R$ -Nb_(1+x)S₂ [47], compared with the much cleaner surface of $2H$ -NbS₂ [14] and other TMDs. Correspondingly, in transport measurements the residual resistivity ratio for $3R$ -Nb_(1+x)S₂ samples is vastly inferior to the stoichiometric $2H$ -NbS₂ [48]. Thus, taking our results together with the literature, we argue that it is the presence of donor-type interstitials that principally distinguishes the electronic and physical properties of $3R$ -Nb_{1+x}S₂ from $2H$ -Nb₂ rather than the difference in stacking arrangement.

If a stoichiometric $3R$ -NbS₂ existed, our DFT calculations suggest it would have a similar Fermi surface to the $2H$ phase and therefore could have similarly interesting properties, potentially including noncentrosymmetric superconductivity.

Unfortunately, stoichiometric $3R$ -NbS₂ is entirely hypothetical and the only thermodynamic bulk phases are $3R$ -Nb_(1+x)S₂ and $2H$ -NbS₂ [18]. However, the monolayer limit provides a third structural form of $1H$ -NbS₂, which has been predicted [12] and observed [49] to enter a CDW phase, although this may be substrate dependent [50] and offers an interesting playground to tune the structural and superconducting instabilities [51].

V. CONCLUSION

In conclusion, the measured Fermi surfaces of $3R$ -Nb_(1+x)S₂ are found to be much smaller than in $2H$ -NbS₂, consistent with a large rigid band shift caused by an extra charge from interstitial Nb. Thus it is the stoichiometry, rather than the stacking sequence, that principally determines the differences in electronic structure and physical properties between the two polytypes. Our high resolution data on $2H$ -NbS₂ reveals kinks in the spectral function but the strength of the coupling is found to be much larger for the sections of bands with Nb $4d_{x^2-y^2,xy}$ character than for the Nb $4d_{3z^2-r^2}$. Our measurements provide an experimental framework for interpreting the two-gap superconductivity and latent CDW in $2H$ -NbS₂, while also giving insight into the absence of these in the $3R$ -Nb_(1+x)S₂.

ACKNOWLEDGMENTS

We thank Niko Tombros and HQ graphene for providing details of sample growth and characterisation. We thank Timur K. Kim for insightful discussions and technical support. We acknowledge Diamond Light Source for time on beamline I05 under Proposal No. CM26443. Z.E.Y. acknowledges Diamond Light Source and CY Cergy-Paris university for Ph.D. studentship support.

-
- [1] J. A. Wilson, F. J. Di Salvo, and S. Mahajan, Charge-Density Waves in Metallic, Layered, Transition-Metal Dichalcogenides, *Phys. Rev. Lett.* **32**, 882 (1974).
- [2] B. Sipos, A. F. Kusmartseva, A. Akrap, H. Berger, L. Forró, and E. Tutiš, From Mott state to superconductivity in 1T-TaS₂, *Nat. Mater.* **7**, 960 (2008).
- [3] K. Rossnagel, On the origin of charge-density waves in select layered transition-metal dichalcogenides, *J. Phys.: Condens. Matter* **23**, 213001 (2011).
- [4] T. Ritschel, J. Trinckauf, K. Koepf, B. Büchner, M. v. Zimmermann, H. Berger, Y. I. Joe, P. Abbamonte, and J. Geck, Orbital textures and charge density waves in transition metal dichalcogenides, *Nat. Phys.* **11**, 328 (2015).
- [5] D. J. Rahn, S. Hellmann, M. Kalläne, C. Sohrt, T. K. Kim, L. Kipp, and K. Rossnagel, Gaps and kinks in the electronic structure of the superconductor $2H$ -NbSe₂ from angle-resolved photoemission at 1 K, *Phys. Rev. B* **85**, 224532 (2012).
- [6] T. Valla, A. V. Fedorov, P. D. Johnson, P.-A. Glans, C. McGuinness, K. E. Smith, E. Y. Andrei, and H. Berger, Quasi-particle Spectra, Charge-Density Waves, Superconductivity, and Electron-Phonon Coupling in $2H$ -NbSe₂, *Phys. Rev. Lett.* **92**, 086401 (2004).
- [7] S. V. Borisenko, A. A. Kordyuk, V. B. Zabolotnyy, D. S. Inosov, D. Evtushinsky, B. Büchner, A. N. Yaresko, A. Varykhalov, R. Follath, W. Eberhardt, L. Patthey, and H. Berger, Two Energy Gaps and Fermi-Surface “Arcs” in NbSe₂, *Phys. Rev. Lett.* **102**, 166402 (2009).
- [8] F. Flicker and J. Van Wezel, Charge order from orbital-dependent coupling evidenced by NbSe₂, *Nat. Commun.* **6**, 7034 (2015).
- [9] J. A. Wilson and A. Yoffe, The transition metal dichalcogenides discussion and interpretation of the observed optical, electrical and structural properties, *Adv. Phys.* **18**, 193 (1969).
- [10] D. Lin, S. Li, J. Wen, H. Berger, L. Forró, H. Zhou, S. Jia, T. Taniguchi, K. Watanabe, X. Xi *et al.*, Patterns and driving forces of dimensionality-dependent charge density waves in $2H$ -type transition metal dichalcogenides, *Nat. Commun.* **11**, 2406 (2020).
- [11] M. Leroux, M. Le Tacon, M. Calandra, L. Cario, M.-A. Méasson, P. Diener, E. Borissenko, A. Bosak, and P. Rodière,

- Anharmonic suppression of charge density waves in $2H$ - NbS_2 , *Phys. Rev. B* **86**, 155125 (2012).
- [12] R. Bianco, I. Errea, L. Monacelli, M. Calandra, and F. Mauri, Quantum enhancement of charge density wave in NbS_2 in the two-dimensional limit, *Nano Lett.* **19**, 3098 (2019).
- [13] C. Heil, S. Ponc e, H. Lambert, M. Schlipf, E. R. Margine, and F. Giustino, Origin of Superconductivity and Latent Charge Density Wave in NbS_2 , *Phys. Rev. Lett.* **119**, 087003 (2017).
- [14] I. Guillam on, H. Suderow, S. Vieira, L. Cario, P. Diener, and P. Rodi ere, Superconducting Density of States and Vortex Cores of $2H$ - NbS_2 , *Phys. Rev. Lett.* **101**, 166407 (2008).
- [15] A. Majumdar, D. VanGennep, J. Brisbois, D. Chareev, A. V. Sadakov, A. S. Usoltsev, M. Mito, A. V. Silhanek, T. Sarkar, A. Hassan, A. O. Karis, R. Ahuja, and M. Abdel-Hafez, Interplay of charge density wave and multiband superconductivity in layered quasi-two-dimensional materials: The case of $2H$ - NbS_2 and $2H$ - $NbSe_2$, *Phys. Rev. Mater.* **4**, 084005 (2020).
- [16] J. Ka mar c ik, Z. Pribulova, C. Marcenat, T. Klein, P. Rodi ere, L. Cario, and P. Samuely, Specific heat measurements of a superconducting NbS_2 single crystal in an external magnetic field: Energy gap structure, *Phys. Rev. B* **82**, 014518 (2010).
- [17] N. Sirica, S.-K. Mo, F. Bondino, I. Pis, S. Nappini, P. Vilmercati, J. Yi, Z. Gai, P. C. Snijders, P. K. Das, I. Vobornik, N. Ghimire, M. R. Koehler, L. Li, D. Sapkota, D. S. Parker, D. G. Mandrus, and N. Mannella, Electronic structure of the chiral helimagnet and $3d$ -intercalated transition metal dichalcogenide $Cr_{1/3}NbS_2$, *Phys. Rev. B* **94**, 075141 (2016).
- [18] W. G. Fisher and M. Sienko, Stoichiometry, structure, and physical properties of niobium disulfide, *Inorg. Chem.* **19**, 39 (1980).
- [19] A. Meerschaut and C. Deudon, Crystal structure studies of the $3R$ - $Nb_{1.09}S_2$ and the $2H$ - $NbSe_2$ compounds: Correlation between nonstoichiometry and stacking type (= polytypism), *Mater. Res. Bull.* **36**, 1721 (2001).
- [20] M. Hoesch, T. Kim, P. Dudin, H. Wang, S. Scott, P. Harris, S. Patel, M. Matthews, D. Hawkins, S. Alcock *et al.*, A facility for the analysis of the electronic structures of solids and their surfaces by synchrotron radiation photoelectron spectroscopy, *Rev. Sci. Instrum.* **88**, 013106 (2017).
- [21] P. Blaha, K. Schwarz, F. Tran, R. Laskowski, G. K. H. Madsen, and L. D. Marks, WIEN2k: An APW+lo program for calculating the properties of solids, *J. Chem. Phys.* **152**, 074101 (2020).
- [22] D. Koller, F. Tran, and P. Blaha, Improving the modified Becke-Johnson exchange potential, *Phys. Rev. B* **85**, 155109 (2012).
- [23] See Supplemental Material at <http://link.aps.org/supplemental/10.1103/PhysRevB.103.155105> for more detailed discussion of the band splittings in the two phases and the orbital characters of the bands, and further details of the fitting analysis and DFT calculations.
- [24] H. Yuan, M. S. Bahramy, K. Morimoto, S. Wu, K. Nomura, B.-J. Yang, H. Shimotani, R. Suzuki, M. Toh, C. Kloc *et al.*, Zeeman-type spin splitting controlled by an electric field, *Nat. Phys.* **9**, 563 (2013).
- [25] X. Zhang, Q. Liu, J.-W. Luo, A. J. Freeman, and A. Zunger, Hidden spin polarization in inversion-symmetric bulk crystals, *Nat. Phys.* **10**, 387 (2014).
- [26] J. M. Riley, F. Mazzola, M. Dendzik, M. Michiardi, T. Takayama, L. Bawden, C. Graner od, M. Leandersson, T. Balasubramanian, M. Hoesch *et al.*, Direct observation of spin-polarized bulk bands in an inversion-symmetric semiconductor, *Nat. Phys.* **10**, 835 (2014).
- [27] R. Suzuki, M. Sakano, Y. Zhang, R. Akashi, D. Morikawa, A. Harasawa, K. Yaji, K. Kuroda, K. Miyamoto, T. Okuda *et al.*, Valley-dependent spin polarization in bulk MoS_2 with broken inversion symmetry, *Nat. Nanotechnol.* **9**, 611 (2014).
- [28] N. Alidoust, G. Bian, S.-Y. Xu, R. Sankar, M. Neupane, C. Liu, I. Belopolski, D.-X. Qu, J. D. Denlinger, F.-C. Chou *et al.*, Observation of monolayer valence band spin-orbit effect and induced quantum well states in MoX_2 , *Nat. Commun.* **5**, 4673 (2014).
- [29] E. Razzoli, T. Jaouen, M.-L. Mottas, B. Hildebrand, G. Monney, A. Pisoni, S. Muff, M. Fanciulli, N. C. Plumb, V. A. Rogalev, V. N. Strocov, J. Mesot, M. Shi, J. H. Dil, H. Beck, and P. Aebi, Selective Probing of Hidden Spin-Polarized States in Inversion-Symmetric Bulk MoS_2 , *Phys. Rev. Lett.* **118**, 086402 (2017).
- [30] H. Yuan, Z. Liu, G. Xu, B. Zhou, S. Wu, D. Dumcenco, K. Yan, Y. Zhang, S.-K. Mo, P. Dudin *et al.*, Evolution of the valley position in bulk transition-metal chalcogenides and their monolayer limit, *Nano Lett.* **16**, 4738 (2016).
- [31] L. Bawden, S. P. Cooil, F. Mazzola, J. Riley, L. Collins-McIntyre, V. Sunko, K. Hunvik, M. Leandersson, C. Polley, T. Balasubramanian *et al.*, Spin-valley locking in the normal state of a transition-metal dichalcogenide superconductor, *Nat. Commun.* **7**, 11711 (2016).
- [32] V. Strocov, Intrinsic accuracy in 3-dimensional photoemission band mapping, *J. Electron Spectrosc. Relat. Phenom.* **130**, 65 (2003).
- [33] V. N. Strocov, E. E. Krasovskii, W. Schattke, N. Barrett, H. Berger, D. Schrupp, and R. Claessen, Three-dimensional band structure of layered $TiTe_2$: Photoemission final-state effects, *Phys. Rev. B* **74**, 195125 (2006).
- [34] Z. El Youbi, S. W. Jung, S. Mukherjee, M. Fanciulli, J. Schusser, O. Heckmann, C. Richter, J. Minar, K. Hricovini, M. D. Watson, and C. Cacho, Bulk and surface electronic states in the dosed semimetallic $HfTe_2$, *Phys. Rev. B* **101**, 235431 (2020).
- [35] The different stacking between the two phases also affects the shape of the Brillouin zone. In the $2H$ phase, it is a simple hexagonal prism, however, in the $3R$ phase the geometry of the 3D Brillouin zone is more complex, as can be seen in Fig. 2(e). Note also that Brillouin zone is twice the height along the c^* axis in the $3R$ phase. For convenience of comparison, we continue to use the familiar notation of K and M also in the $3R$ phase [e.g., in Fig. 1(f)], even though these are not formal high-symmetry points in this case. Similarly, we draw a simple hexagonal Brillouin zone in Figs. 2(f) and 2(g) that corresponds to a surface-projected Brillouin zone.
- [36] C. Heil, M. Schlipf, and F. Giustino, Quasiparticle GW band structures and Fermi surfaces of bulk and monolayer NbS_2 , *Phys. Rev. B* **98**, 075120 (2018).
- [37] The stoichiometry was determined from EDX measurements provided by HQ Graphene, as described in the Supplemental Material.
- [38] P. Diener, M. Leroux, L. Cario, T. Klein, and P. Rodi ere, In-plane magnetic penetration depth in NbS_2 , *Phys. Rev. B* **84**, 054531 (2011).
- [39] V. G. Tissen, M. R. Osorio, J. P. Brison, N. M. Nemes, M. Garca-Hernandez, L. Cario, P. Rodi ere, S. Vieira, and

- H. Suderow, Pressure dependence of superconducting critical temperature and upper critical field of $2H$ - NbS_2 , *Phys. Rev. B* **87**, 134502 (2013).
- [40] C. Wen, Y. Xie, Y. Wu, S. Shen, P. Kong, H. Lian, J. Li, H. Xing, and S. Yan, Impurity-pinned incommensurate charge density wave and local phonon excitations in $2H$ - NbS_2 , *Phys. Rev. B* **101**, 241404(R) (2020).
- [41] K. Rossnagel, O. Seifarth, L. Kipp, M. Skibowski, D. Voß, P. Krüger, A. Mazur, and J. Pollmann, Fermi surface of $2H$ - NbSe_2 and its implications on the charge-density-wave mechanism, *Phys. Rev. B* **64**, 235119 (2001).
- [42] M. D. Johannes, I. I. Mazin, and C. A. Howells, Fermi-surface nesting and the origin of the charge-density wave in NbSe_2 , *Phys. Rev. B* **73**, 205102 (2006).
- [43] M. D. Johannes and I. I. Mazin, Fermi surface nesting and the origin of charge density waves in metals, *Phys. Rev. B* **77**, 165135 (2008).
- [44] F. Flicker and J. van Wezel, Charge order in NbSe_2 , *Phys. Rev. B* **94**, 235135 (2016).
- [45] P. Hofmann, I. Y. Sklyadneva, E. Rienks, and E. Chulkov, Electron-phonon coupling at surfaces and interfaces, *New J. Phys.* **11**, 125005 (2009).
- [46] Y. Nishio, M. Shirai, N. Suzuki, and K. Motizuki, Role of electron-lattice interaction in layered transition metal dichalcogenide $2H$ - NbS_2 . I. Phonon anomaly and superconductivity, *J. Phys. Soc. Jpn.* **63**, 156 (1994).
- [47] T. Machida, Y. Kohsaka, K. Iwaya, R. Arita, T. Hanaguri, R. Suzuki, M. Ochi, and Y. Iwasa, Orbital-dependent quasiparticle scattering interference in $3R$ - NbS_2 , *Phys. Rev. B* **96**, 075206 (2017).
- [48] A. Niazi and A. Rastogi, Low-temperature resistance minimum in non-superconducting $3R$ - $\text{Nb}_{1+x}\text{S}_2$ and $3R$ - Ga_xNbS_2 , *J. Phys.: Condens. Matter* **13**, 6787 (2001).
- [49] H. Lin, W. Huang, K. Zhao, C. Lian, W. Duan, X. Chen, and S.-H. Ji, Growth of atomically thick transition metal sulfide films on graphene/ $6H$ - SiC (0001) by molecular beam epitaxy, *Nano Res.* **11**, 4722 (2018).
- [50] R.-M. Stan, S. K. Mahatha, M. Bianchi, C. E. Sanders, D. Curcio, P. Hofmann, and J. A. Miwa, Epitaxial single-layer NbS_2 on $\text{Au}(111)$: Synthesis, structure, and electronic properties, *Phys. Rev. Mater.* **3**, 044003 (2019).
- [51] A. Devarakonda, H. Inoue, S. Fang, C. Ozsoy-Keskinbora, T. Suzuki, M. Kriener, L. Fu, E. Kaxiras, D. Bell, and J. Checkelsky, Clean 2D superconductivity in a bulk van der Waals superlattice, *Science* **370**, 231 (2020).